Bulletin of the Seismological Society of America, Vol.99, No.4, xxx-xxx, August 2009

Estimation of the high-frequency radiation of the 2000 Tottori (Japan) earthquake based on a dynamic model of fault rupture: Application to the strong ground motion simulation

by Nelson Pulido and Luis A. Dalguer

Abstract In the present study we investigate the high frequency (HF) radiation mechanism of the 2000 Tottori earthquake, Japan, based on a 3D spontaneous fault rupture dynamic model. We generalize the model of HF radiation of a suddenly stopping circular crack (Madariaga, 1977; Boatwright, 1982), to the radiation from a general 3D rupture in a planar fault, where HF is radiated during gradual changes of rupture velocity at the rupture front. Local rupture velocity changes are expressed as the divergence of local rupture velocity vectors, which are derived from gradients of rupture times from the dynamic model. Our numerical model of the Tottori earthquake indicates that rupture velocity changes are largely induced by barriers (locally stronger fault sections) across the fault plane, and that HF radiation mainly originates within asperities (large stress drop regions), in areas where the product of dynamic stress drop and rupture velocity changes is maximum. We develop a strong ground motion simulation methodology that incorporates HF radiation inferred from a dynamic fault rupture model. Using this methodology we investigate the HF radiation of the Tottori earthquake by inverting observed near-source acceleration envelopes of the earthquake. Our inversion results corroborate that HF radiation originates within asperities, and show that significant HF radiation represents no more than a 20% of the total asperity area. Our results show that the incorporation of a directivity factor, on the basis of a well-defined physical rupture model, to the radiation pattern, leads to a significant improvement in fitting of observed ground motions. Our simulated near-source strong ground motions of the Tottori earthquake are also able to reproduce the ω^{-2} radiation theoretically predicted in 2D dynamic fault rupture models.

Introduction

In the last two decades, the large number of earthquake kinematic slip models that have become available, have substantially contributed to advance our understanding of different aspects related to earthquake mechanisms and near source ground motion. Most available source models are based only on the low frequency seismic radiation, mainly because of the difficulty in describing deterministically the high frequency generation process, very complex by nature. To partially overcome this problem several studies have used envelopes of near-source high-frequency records to investigate the process of high frequency radiation. Some of these studies locate the radiation of high frequency near boundaries of large low-frequency slip regions (Zeng et al., 1993; Kakehi and Irikura, 1996a; Nakahara, 1998, 2002), while others locate intuitively the HF radiation near fault-plane discontinuities (Kakehi et al., 1996b; Kakehi and Irikura, 1997).

However as these studies are typically based on nearly uniform fault rupture models, the influence of a heterogeneous fault rupture process on the HF ground motion radiation has not been fully investigated. Theoretical earthquake physic models show that in dynamic rupture with a circular rupture front, strong variations of the rupture velocity at the crack boundaries (stopping phases) play a very important role in the radiation of high frequency from the source (Madariaga, 1977, 1983). For finite fault ruptures, a gradual acceleration or deceleration of the rupture front during the rupture propagation may have a large contribution to the HF ground motion generation (e.g., Achenbach and Harris, 1978; Spudich and Frazer 1984; Cocco and Boatwright, 1993; Sato 1994).

We invoke some of the spirit of these earthquake physic models to investigate the potential contribution of rupture velocity heterogeneity on the HF radiation from the source for the 2000 Western Tottori prefecture M7 earthquake (Japan) (Figure 1). Using a spontaneous dynamic rupture simulation of this earthquake as well as inversion of observed near-source envelopes, we show in this paper that HF is radiated within regions in the fault plane where the product of stress drop and rupture velocity changes is large, and that significant HF radiation during the Tottori earthquake represented no more than a 20% of the total asperity area (patches of large stress drop).

In the following we will present our dynamic rupture modeling approach and corresponding results, which we use to estimate areas of HF radiation. These will be contrasted with independent estimates of HF radiation from near-source envelope inversions. Finally we will present a methodology for the simulation of broadband strong ground motion that incorporates a dynamic model of spontaneous fault rupture.

Dynamic fault rupture process

Dynamic Model

We investigate a spontaneous dynamic fault rupture process of Tottori earthquake by using a newly developed numerical method of fault rupture dynamics, named Staggered-grid split-node (SGSN). The SGSN method (Dalguer and Day 2007) is an adaptation of the traction-at-split-node method of Day (1982) to a velocity-stress staggered-grid finite difference scheme. The SGSN implementation introduces velocity as well as stress discontinuities at the fault plane via split nodes. The traction-at-split-node methods are able to solve a 3-D spontaneous fault rupture model with the same level of accuracy compared to the Boundary Integral method (Day et al., 2005).

For the dynamic model of the Tottori earthquake we use a grid size of 0.1 km and a time step of 0.0065s (331 grids along strike and 211 grids along dip). These parameters allow us to adequately resolve the spontaneous fault rupture process, as well as the wave propagation up to 5Hz. The fault model is a vertical fault plane striking N150°E, with a length of 33 km and a width of 21 km. The fault upper edge is located a 0.2 km depth. The plane is embedded in a 1-D structure velocity model used for earthquake location in the region (Table 1), and the size of the 3D model domain is 62.8 km by 50 km, respectively parallel, and perpendicular to the fault plane and 26.4 km of depth (Figure 2). In order to start the rupture we set an initial crack of 2 km of diameter, located at a 13.4 km depth. Parameters of the dynamic model are summarized in Table 2.

Friction Law

We use a simple slip weakening friction law in which the shear stress τ at the fault surface is given by:

$$\tau(l) = \begin{cases} \tau_s - (\tau_s - \tau_d) l / d_c & l < d_c \\ \tau_d & l \geq d_c \end{cases} \tag{1}$$

where τ_s is the static yielding stress, τ_d is the dynamic yielding stress, l is the slip and d_c is the critical slip-weakening distance (Ida, 1972; Andrews, 1976).

Initial values of dynamic stress drop ($\Delta\sigma = \tau_o - \tau_d$), and strength excess ($\tau_e = \tau_s - \tau_o$), where τ_o is the initial shear stress, are estimated from the spatio-temporal stress histories from a kinematic slip model of the Tottori earthquake (Iwata et. al. 2000), by solving the elasto-dynamic equations of fault motion (Dalguer et. al. 2002; Zhang et. al. 2003). The dynamic stress drop is adjusted iteratively by performing several spontaneous dynamic fault rupture simulations. At each iteration the stress drop values are corrected by the ratio of kinematic to dynamic final slip (Dk/Dd). This procedure is repeated until the ratio Dk/Dd closely converges to 1 in areas of large slip. In this way we constraint our dynamic model to generate the same final slip of the kinematic model by allowing a heterogeneous rupture velocity propagation. The strength excess is then calculated by trial and error by performing spontaneous dynamic models that generate a total rupture time equivalent to the rupture time of the kinematic model. Initial strength excess values are obtained from the kinematic model by a similar procedure to the one applied for the stress drop.

The estimation of the critical slip distance (d_c) has been a subject of very active research in recent years. Many researchers have attempted to estimate d_c from seismic radiation (e.g., Ide and Takeo, 1997; Pulido and Irikura, 2000; Mikumo et al., 2003; Zhang et al., 2003) as well as from laboratory experiments (Ohnaka 2000). Some studies identified a correlation between d_c (or fracture energy) and the final fault slip (Pulido and Irikura, 2000; Mikumo et al., 2003; Tinti et al., 2005 and Rice 2006). A similar result was obtained by a fracture mechanics approach based on laboratory results (Ohnaka 2000 and 2003). Following these studies we set a heterogeneous d_c distribution across the fault plane as 20% of the final slip of the Tottori earthquake.

Asperities and barriers of the Tottori earthquake

We applied the SGSN method to obtain a spontaneous dynamic fault rupture of the Tottori earthquake. Figure 3a shows a comparison between the final slip of the dynamic model in a grayscale, with the final slip of the kinematic model depicted by white contour lines. As seeing in this figure, the two models closely follow the same final slip, which confirms the efficacy of the iterative procedure explained in the previous section. Figure 3b shows the dynamic stress drop distribution (in a color scale), obtained from the final dynamic model. The stress drop reaches a value of 20Mpa in a region 8 km above the hypocenter. As a general feature we see that large stress drop regions, which we will subsequently refer to "asperities" (large pre-stress regions), are surrounded by areas of zero or negative stress drops. This characteristic has been observed in numerical simulations of sub-surface earthquakes (e.g., Dalguer et al., 2008). Negative stress drops are also found in areas towards the edges of the fault, where the rupture decelerates or stop. For the Tottori earthquake, asperities are defined as the areas enclosed by a stress drop larger than 5MPa, which approximately correspond to a 25% of the total fault area. This asperity definition approximately follows the model defined by Somerville et. al. (1999) and Dalguer et. al. (2008). In Figure 3b we overlapped as well the strength excess distribution across the fault plane by white contour lines. We will denominate "barriers" to areas within the fault plane with larger strength excess than its surroundings. For the Tottori earthquake we may identify a strong barrier of 2Mpa located approximately 5 km above the hypocenter. This barrier plays a very important role in controlling the rupture process of the Tottori earthquake as we show in the following sections. Strength excess also has increasingly large values towards the edges of the fault, which force the rupture to stop within a total rupture time comparable with the rupture time of the kinematic model.

Rupture Velocity of the Tottori earthquake

From the results of the dynamic rupture simulation we obtain the position of the rupture front time at every location across the fault plane, as depicted by the black contour lines in Figure 4a. To evaluate the rupture velocity vectors at every grid point within the fault plane we first calculate the rupture slowness vectors ($\vec{u}$) defined as the gradient of rupture times from the dynamic model across the fault plane (t), along the fault strike and dip directions (denoted by the unit vectors $\hat{x}$ and $\hat{y}$ respectively);

$$\vec{u} = \nabla t = \frac{\partial t}{\partial x}\hat{x} + \frac{\partial t}{\partial y}\hat{y} \tag{2}$$

The rupture velocity vector ($\vec{V}_{r_{ij}}$) at a particular point along the fault strike (i) and dip (j) is obtained as,

$$\vec{V}_{r_{ij}} = \frac{\cos\varphi_{ij}}{\left|\nabla t\right|_{ij}}\hat{x} + \frac{\sin\varphi_{ij}}{\left|\nabla t\right|_{ij}}\hat{y} \tag{3}$$

where φ_{ij} is the angle between $\vec{V}_{r_{ij}}$ and $\hat{x}$ as follows:

$$\varphi_{ij} = \tan^{-1}(\nabla t_{ij}\cdot\hat{y} / \nabla t_{ij}\cdot\hat{x}) \tag{4}$$

In Figure 4a we plot the distribution of rupture velocity amplitude across the fault plane (in grey scale). From this figure we might observe that the rupture velocity is very heterogeneous, in contrast with kinematic models of the source where rupture velocity is nearly constant. In average the rupture velocity is 2.98 km/s, which means approximately an 84% of the mean S-wave velocity. However, locally the rupture velocity largely exceeds the average S-wave velocity, specially along the strike direction at the hypocenter where the rupture reaches supershear values within 0.5s, as well as in a region 8 km above the hypocenter (Figure 4a). Local super-shear rupture velocity can be difficult to identify from kinematic source inversions and observed ground motion studies, but dynamic rupture models show that it is very likely to occur in a fault with heterogeneous stress distribution (e.g. Day 1982). In Figure 4a we overlapped the strength excess values above 2MPa (white contour lines), in order to explore its relationship to the rupture velocity. We see that a strong barrier located above the hypocenter has a clear effect on the deceleration, bending and focusing of the rupture front. Immediately below this barrier the rupture strongly decelerates and surrounds the barrier by propagating clockwise and counterclockwise to focus at the opposite side. Figures 5a and 5b show the rupture velocity vectors obtained by equation (3) and sampled at every kilometer across the fault plane, as well as a close-up of the vectors in a region above the hypocenter at a 0.2 km grid spacing. Rupture front rotation around the barrier (gray shaded area) and its focusing are remarkable features shown by these figures. A similar rupture front focusing produced by locally stronger fault sections has been documented in the literature (Das and Kostrov 1983, Fukuyama and Madariaga 2000, Dunham et. al. 2003, and Kato 2007). The rupture front focusing greatly contributes to the HF seismic radiation from the fault as we will describe in the next section. Another interesting feature of the rupture velocity field are the discontinuities observed at depths of 2km and 16km (Figures 4a and 4b), which correspond to the interface between different layers of the structure velocity model used for the dynamic simulation. However in the actual subsurface velocity structures we would expect smoother changes of the velocity at the interfaces, and therefore weaker rupture velocity discontinuities.

Rupture Velocity and rupture mode

To illustrate the 3D characteristics of fault rupture, as well as the close relationship between the rupture mode and rupture velocity, we calculate a coefficient (*rup*) that is proportional to the angle between the fault slip direction and the rupture propagation direction φ_{ij} ($|\varphi_{ij}|\leq\pi$), as follows;

$$rup = \left|1 - 2\left|\varphi_{ij}\right| / \pi\right| \tag{5}$$

Equation 5 takes a value of 1 when the rupture propagates in pure Mode II (when the slip and rupture front are aligned), and 0 when the rupture propagates in pure Mode III (when the slip and rupture front are perpendicular). The values in between represent a mixed Mode II and III fault rupture propagation. In our model of the Tottori earthquake the slip direction is almost parallel to the fault strike for all grids, and therefore φ_{ij} approximately corresponds to the angle that the rupture front makes with the horizontal. In Figure 4b we plot the value of the *rup* coefficient across the fault plane. We may observe that the rupture propagates in Mode II in a region adjacent to the hypocenter where the fault ruptures bilaterally along the strike, as well as at the region 8 km above the hypocenter where the rupture front surrounds the 2MPa barrier previously described. A comparison between Figures 4a and 4b shows that the areas where rupture velocity reach super-shear values approximately correspond with a Mode II rupture. On the other hand, areas were rupture propagates in a sub-shear range, correspond as expected to a rupture Mode III or a mix of ruptures Modes II and III. An interesting feature may be observed at the rupture front focusing region (labeled from points A to B in Figure 4b), where a Mode II rupture front propagating co-linearly to the fault strike, suddenly encounters a Mode III rupture front propagating up-dip at the opposite side (Figure 4b, 5a,b).

Estimation of High Frequency Radiation based on a dynamic model

Madariaga (1977) and Achenbach and Harris (1978) theoretically demonstrated that HF frequency radiation from the source is proportional to sudden rupture velocity variations, which produce stress intensity changes at the rupture front. Madariaga (1977) solved this problem for semi-infinite in-plane and antiplane ruptures, as well as a suddenly stopping circular fault. In this study we generalize these models to the HF radiation arising from gradual changes in rupture velocity from a 3D fault rupture. Following Madariaga (1977) we evaluate the stress concentrations at the rupture front by using the stress intensity factor K^*_{ij}, defined at the ij subfault as follows;

$$K^*_{ij} = k \Delta\sigma_{ij} L^{1/2}_{ij} \tag{6}$$

Where k is a factor that depends on the rupture type (in-plane or anti-plane) and rupture history, $\Delta\sigma_{ij}$ is the stress drop and L_{ij} is the rupture length measured as the distance from the hypocenter to the ij subfault.

In order to calculate the HF radiation from the source we also must evaluate the changes in rupture velocity at the rupture front. To get a complete description of the instantaneous rupture velocity change at every location within the fault, we need to evaluate the gradient tensor of the rupture velocity field obtained from our 3D dynamic model of fault rupture. This implies that the rupture velocity change is a second order tensor. In this paper for simplicity we will only use a scalar definition of the rupture velocity changes (ΔVr_{ij}) as the divergence of the rupture velocity field as follows:

$$\Delta V_{r_{ij}} = \nabla \cdot \vec{V}_{r_{ij}} \tag{7}$$

From equations (3) and (7) we can obtain the local rupture velocity changes as:

$$\Delta V_{r_{ij}} = \frac{\partial(\cos\varphi_{ij} / \left|\nabla t\right|_{ij})}{\partial x} + \frac{\partial(\sin\varphi_{ij} / \left|\nabla t\right|_{ij})}{\partial y} \tag{8}$$

Since ∇t and φ are functions of x and y we can obtain the ΔV_r distribution across the fault plane by solving numerically equation (8). In order to get an approximation to the local values of rupture velocity change, we multiply the divergence of the rupture velocity vectors in equation (8), which represent changes of V_r per unit length, by the grid size. From equation 8 we may observe that the divergence of ΔVr_{ij} actually corresponds to the trace of the rupture velocity gradient tensor.
To calculate the high frequency radiation from the source, we define the variable Ω_{ij} as the product of stress intensity factor and rupture velocity changes across the fault plane as follows:

$$\Omega_{ij} = \left| K^*_{ij} \Delta V_{r\,ij} \right| \tag{9}$$

The variable Ω_{ij} approximately corresponds to the spectral level of far-field radiation of an acceleration pulse generated by a sudden rupture velocity change at the rupture front (Madariaga 1977, Boatwright 1982). Based on the above assumptions we might envision a model composed of many of these rupture velocity changes at the rupture front, as a way to represent the HF ground motion radiation from a 3D fault rupture as schematically shown in Figure 6. In this Figure we show an image of an irregularly growing fault rupture and the associated stress concentrations at the rupture front deriving from rupture velocity changes.

High frequency radiation during the Tottori earthquake from a dynamic model

We calculated the high frequency radiation across the fault plane during the Tottori earthquake by applying equation (8). In Figure 7a we plot the rupture velocity changes across the fault in a color scale. We may observe very heterogeneous positive as well as negative changes in local rupture velocity. The positive rupture velocity changes correspond to an acceleration or “spreading” of the rupture front, whereas the negative changes correspond to a deceleration or “focusing” of the rupture front. Although the rupture velocity change is close to zero for large areas across the fault plane (namely a uniform rupture propagation), locally the rupture front experiences strong accelerations and decelerations. The most prominent rupture velocity changes are found in a region immediately below the 2MPa barrier above the hypocenter, where the rupture experience a strong deceleration, as well as in the rupture front focusing region above the hypocenter (the elongated blue region labeled from points A to B). More regions of strong decelerations can be observed towards the end of other super-shear rupture velocity patches (Figures 4a and 7a). Within these patches we may observe very heterogeneous rupture velocity changes in contrast to the smoother changes within sub-shear rupture propagation areas.
Finally we calculate the local high frequency radiation distribution across the fault plane using equation 9 (Figure 7b). In this Figure we overlap the stress drop distribution as black contour lines. We can observe that the region responsible for the largest HF radiation is located 8 km above the hypocenter where this product is maximum. This region is characterized by having at the same time a large dynamic stress drop as well as strong rupture velocity changes. Note that the rupture front focusing area above the hypocenter has a large contribution to the HF radiation from the fault. This result suggest that high frequency is mostly radiated from regions where a strong dynamic stress drop is overlapped with large local variations in rupture velocity, namely a rough rupture propagation. On the other hand regions in the fault plane with a smooth rupture propagation, like most areas propagating in a sub-shear regime, do not radiate high frequencies even within areas with large stress drops (above 10 MPa).

Estimation of HF radiation from inversion of observed records

In order to test the HF radiation model proposed in the previous section we obtain an independent estimate of the HF radiation of the Tottori earthquake by applying an inversion procedure to fit observed envelopes of the two horizontal components (EW, NS) at six near-source strong motion recordings of the earthquake from the K-NET and KiK-net networks (Aoi et. al. 2004). We set the rupture velocity changes across the fault plane (ΔV_r), and the stress intensity coefficient k (equation 6), as model parameters for inversion. Before inversion observed seismograms are de-convolved to a hard-rock site condition (β=3.5 km/s) by the respective site amplification function at each station (for details see Appendix A), and band-passed filtered between 1 and 30Hz. We then evaluate the ground motion envelopes as the RMS average of corrected acceleration waveforms and their Hilbert transform. We simulate HF waveforms at the target sites for a hard-rock geological condition as we will later describe in the strong motion simulation section of this paper, and then evaluate their envelopes as described previously.

In order to reduce the number of parameters for inversion we re-sampled the original dynamic model to a grid size of 1 km, yielding a grid mesh of 33 grids along strike and 21 grids along dip, and only consider grids shallower than 14 km. We further reduced the number of model parameters by restraining the inversion to areas within the fault plane where ΔV_r from the dynamic model is larger than 0.6 km/s, in order to only concentrate in regions with a large potential contribution to the HF radiation. This choice yielded a total of 188 parameters for inversion. For the calculation of HF ground motions in addition to the ΔV_r values from inversion, we use the sampled ΔV_r values from the dynamic model for the remaining areas (ΔV_r from dynamic model $\leq$ 0.6 km/s and subfaults deeper than 14 km). The stress drop is calculated as the average of the values from the dynamic model within every square kilometer and is fixed during inversion. We also fixed the value of f_{max} to 10Hz, estimated from a visual inspection of site effects corrected acceleration Fourier spectra for all stations. All the other parameters for the simulation of strong motions are summarized in Table 3.

To estimate the best model parameters we used genetic algorithms (Chipperfield et. al. 1994), and implemented a parallel version using Matlab MPI (Kepner and Ahalt 2004). We set the interval of variation of ΔV_r for inversion between 4*ΔV_r - 0.46 and ΔV_r /4 +0.11 (where ΔV_r's are the maximum rupture velocity changes values within every square kilometer, and these boundaries where chosen to yield search domains of similar area above and below ΔV_r), and the interval of variation for k between 0.05 and 0.4. We further constrained the upper level of ΔV_r for inversion to be smaller than the maximum S-wave velocity in the source region (β_{max}), to avoid a singularity in the calculation of the directivity factor in equation (12). We select the following cost function to be minimized by the inversion;

$$\mathrm{var} = \sum_{j=1}^{N}\left[1-\frac{2\sum_{k=1}^{n} O_{jk}S_{jk}}{\sum_{k=1}^{n} O_{jk}^2+\sum_{k=1}^{n} S_{jk}^2}\right] \tag{10}$$

where O_{jk} and S_{jk} are the observed and simulated envelopes at station j and time sample k, and N is the total number of components. We set the total number of generations to 500 as a stopping criterion of the inversion. The total number of source models evaluated during inversions was ~817.000.

The results of the inversion are displayed in Figure 8. In Figure 8a we show the ΔV_r values obtained from the dynamic model. In Figure 8b we show the inverted ΔV_r values, and in Figure 8c we plot the distribution of the HF coefficient Ω across the fault plane (eq. 9), by using the inverted ΔV_r values. We can observe that although the main features from the dynamic model are also observed in the inversion results, particularly the rupture front focusing region above the hypocenter, the inverted ΔV_r values largely fluctuates around the ΔV_r values inferred from the dynamic model, in order to fit the observed envelopes. From inversion we obtained a value for the stress intensity coefficient k equal to 0.13 (equation 6), which is similar to the value used for SH waves by Boatwrigth (1982), but smaller than the values obtained by Madariaga (1979) for circular cracks.

In Figure 9 we show the comparison between the observed and simulated envelopes for the two horizontal components at the target sites (red and dark blue lines respectively). We may observe a good fitting of the envelopes for most of the components (total variance reduction [eq. 10] is 11%). A significant difference in amplitude is observed in the NS component of the SMNH10 station were probably the site effect correction to the observed waveform is inappropriate. In Figure 9 we also plotted for comparison the envelopes calculated by assuming the radiation pattern without the directivity effects (equation 13). The results are shown as light blue dash lines. We may observe that neglecting the directivity effect in the radiation pattern results in an under-estimation of the amplitudes at stations located near or around the fault nodal plane along the strike (OKYH08, OKYH09, SMN002, SMNH10). For stations located in a direction perpendicular to the fault plane (SMNH02, TTRH04), the envelope amplitudes are almost unaffected by the directivity factor defined in equation (12).

Our inversion results show that significant HF radiation during the Tottori earthquake was confined to an area within asperities representing no more than a 20% of the total asperity area (Figure 8c). This value was obtained as the percentage of asperity area corresponding to Ω values larger than 1.5 times the average Ω within asperities. This result has a very important implication for the prediction of the strong ground motion for future earthquakes, as many current approaches used for strong motion simulation assume that the low as well as high frequencies are radiated from the entire asperity area, without an appropriate consideration about the heterogeneity of rupture propagation.

Strong Motion simulation

Strong motion simulation methodology

Many methodologies for the broadband strong motion simulation have been developed in the last decade, based on kinematic finite fault rupture models. Some of them are based on slip models composed of several asperities of regular shape (Kamae et al. 1998, Pitarka et. al. 2000, Miyake et. al. 2003, Pulido and Kubo 2004, Pulido et. al 2004 and Sorensen et. al. 2007a,b), others are based on a fractal slip distribution (Herrero and Bernard 1994, Irikura and Kamae 1994, Zeng and Anderson 1996, Hartzell et al. 1999 and 2005, Hisada 2000 and 2001), while others use a random-field complex slip (Mai and Beroza 2003, Hartzell et. al. 2005, and Liu et. al. 2006). Although these kinematic-based models represent very helpful tools for the estimation of the broadband near-source ground motions from finite faults, they are typically based on the assumption of a nearly uniform fault rupture propagation, which can produce an over-estimation of the directivity effect in near-fault ground motions as a result of a coherent summation of subfaults, and might be inappropriate to address the study of HF ground motion radiation from the source.

Recently dynamic and pseudo-dynamic fault rupture models have been developed to simulate near-fault ground motions, thus introducing a more physically based fault rupture process (e.g., Miyatake, 2000; Dalguer et al., 2001; Guatteri et al., 2003 and 2004, Oglesby and Day 2002; Aochi and Olsen, 2004; Hartzell et al., 2005; Dunham and Archuleta 2005; Page et al., 2005). However the application of these methodologies has been mostly limited to the low frequencies.

In the present work we use a full spontaneous rupture dynamics approach to investigate the high frequency radiation mechanism from a fault rupture. Based on this study we develop a procedure for the simulation of broadband strong ground motion as described below.

We calculate broadband ground motions in a low and high frequency bands separately and add them in time domain. The low frequency waveforms are obtained by calculating the wave propagation from the dynamic fault rupture model within the SGSN grid domain. The high frequency waveforms are calculated as suggested in a previous section, as the far field ground motion radiation of many rupture velocity changes at the rupture front for a 3D fault rupture. To implement this model we subdivide the fault plane into a large set of subfaults of equal area and uniformly distributed, whose rupture time and spectral radiation is specified by our spontaneous dynamic model of fault rupture. Following equation 46 of Madariaga (1977), which represents the radiation from a 3D rupture obtained by applying the geometrical theory of diffraction to 2D rupture solutions (in-plane and anti-plane), we define the far-field S-wave acceleration spectra a_{ijk}^{m} radiated by each sub-event ij, at station k, and for the m component (EW or NS) as,

$$a_{ijk}^{m}(f) = \frac{R_{\theta\phi\psi}^{m} D\,\Omega_{ij} e^{\pi f R_{ijk}/Q(f)\beta} P(f)\,F\,C_I}{R_{ijk} L_{ij}^{-1/2} \rho\beta^2}\; E(f) \tag{11}$$

where f is the frequency, Ω_{ij} is the HF radiation factor defined in equation 9, D is a diffraction factor of the waves radiated at the rupture front, obtained as an average for SH waves (see Figure 4 in Achenbach and Harris 1978), and ρ and β are the average density and shear wave velocity around the source area. We have incorporated an anelastic attenuation term $Q(f)$, a geometrical spreading R_{ijk} from sub-event ij to station k, as well as a high frequency ground motion attenuation filter P for frequencies above f_{max} ($P = \left[1 + \left[f/f_{\max}\right]^{a}\right]^{b}$), whose strength is controlled by factors a and b. We also include L_{ij}, the rupture length defined in equation 6, as a simple way to account for the 3D effect of the curvature of the rupture front into the geometrical spreading of the waves in the far field (see equation 46 in Madariaga 1977). In a future study we may consider in more detail this 3D geometrical diffraction effect. F is a factor accounting for the free surface and transmission/reflection coefficients (2 for SH waves), and C_I is the impedance ratio between the ij source and site k ($C_I = \sqrt{\rho_{ij}\beta_{ij}/\rho_k\beta_k}$). $R_{\theta\phi\psi}^{m}$ is the radiation pattern coefficient for the m component, obtained by modulating a frequency dependent double couple radiation pattern R^m, by a directivity factor (Madariaga 1977, Boatwright 1982),

$$R_{\theta\phi\psi}^{m} = \frac{R^{m}(\theta,\phi,f)}{1 - \Delta V_{r_{ij}} \cos(\psi) / \beta_{\max}} \tag{12}$$

where θ and ϕ are the subfault-station takeoff angle and azimuth, ψ is the angle between the take-off ray and the rupture velocity vector at the *ij* subfault, and ΔV_{rij} is the rupture velocity change defined in equation 8, and β_{max} is the maximum S-wave velocity in the source region. The radiation pattern R^m is assumed to have a frequency dependence by applying a linear transition from a double couple radiation pattern F^m for frequencies below f_1, to a completely uniform radiation pattern F^{ave} for frequencies above f_2, to account for the observed scattering effect from a heterogeneous structure in the near-source region (Pulido and Kubo 2004, and Pulido et al. 2004),

$$
\begin{aligned}
R^m &= F^m && \text{for} \quad f \le f_1 \\
R^m &= F^m + \frac{(f - f_1)}{(f_2 - f_1)}(F^{ave} - F^m) && \text{for} \quad f_1 < f < f_2 \\
R^m &= F^{ave} && \text{for} \quad f \ge f_2
\end{aligned}
\tag{13}
$$

and we set f_1=1 Hz and f_2=5Hz for the Tottori earthquake. F^m is the radiation pattern of a double couple in terms of geographical coordinates (EW and NS), obtained by adding the projections of SH and SV waves along the EW and NS axes, from equation 4.88 of Aki and Richards (2002),

$$
\begin{aligned}
F^{ew} &= \left| F_{SH}\cos\phi + F_{SV}\cos\theta\sin\phi \right| \\
F^{ns} &= \left| -F_{SH}\sin\phi + F_{SV}\cos\theta\cos\phi \right|
\end{aligned}
\tag{14}
$$

where F_{SH} and F_{SV} are the SH and SV radiation patterns of a double couple calculated based on the fault mechanism (eqs. 4.90 and 4.91, Aki and Richards 2002). Finally F^{ave} is the rms average radiation pattern for the total S wave calculated as in Boore and Boatwright (1984), and divided by $\sqrt{2}$ to account for the partition of the ground motion energy into two horizontal components:

$$
F^{ave} = 1/\sqrt{2}\left[\sum_{i=SH,SV}\left(\frac{\int_{\pi/2}^{\pi}\int_{0}^{2\pi} F_i^2 \sin\theta \, d\phi \, d\theta}{\int_{\pi/2}^{\pi}\int_{0}^{2\pi} \sin\theta \, d\phi \, d\theta}\right)\right]^{1/2}
\tag{15}
$$

For a vertical strike-slip fault and for rays departing in the upper focal sphere F^{ave} yields a value of 0.45.

In equation 11 $E(f)$ is the Fourier spectra of a random phase acceleration time function of sub-events, whose envelope (*env*) is calculated from an empirical regression obtained from observed accelerograms of earthquakes with moment magnitudes between 4 and 5.5, to implement the high frequency waveform broadening effect due to scattering (Horike 2006). The envelope is a function of the focal distance (R_{ijk}, in km), depth (h_{ij}, in km) and the Brune corner frequency f_{cij} ($f_{cij} = 0.49\beta\left(\Delta\sigma_{ij}/Mo_{ij}\right)^{1/3}$, in SI units, where Mo_{ij} is the *ij* subfault seismic moment),

$$
env(t) = t^{1.25} e^{-6.25tT_w^{-1}} \tag{16}
$$

$$
T_w = 2f_{cij}^{-1} + 0.34(R_{ijk} - 15) - 0.0012h_{ij} \tag{17}
$$

where t is time (s), and T_w is the envelope width. The envelopes are normalized by its peak value.

The total high frequency ground motion at a particular station (k) and component (m) is calculated by adding up the contribution from all sub-events,

$$
A_k^m(t) = \sum_{i=1}^{Ns}\sum_{j=1}^{Nd} a_{ijk}^m(t - t_{ijk}) \tag{18}
$$

where $a_{ijk}^m(t)$ is the elementary crack waveform obtained as the inverse Fourier transform of the spectra outlined from equations (11) to (17), N_s and N_d are the number of subfaults along the strike and dip, and t_{ijk} is the wave arrival time at station k radiated from the *ij* subfault, calculated by adding the subfault rupture times from the dynamic model and the subfault-station travel time for a 1D velocity structure (Table 1).

Simulated ground motions of the Tottori earthquake

In Figure 10a we show a comparison between the observed and simulated HF accelerograms (1 to 30 Hz), corresponding to selected envelopes from Figure 9. We notice that the overall observed ground motions amplitudes and durations are well reproduced. We must note that our ground motion simulations in this paper only include the S-waves. However with a small modification we can easily include the contribution of P-waves.

In Figure 10b we show a comparison between observed and simulated broadband (BB) frequency accelerograms (0.1 to 30Hz) for stations within the grid domain of our dynamic model of the Tottori earthquake. We did not include the farthest stations used for the HF inversion in order to reduce the computation time of the dynamic model. We calculated BB accelerograms by adding the HF seismograms in Figure 10a and the low frequency (0.1 to 1 Hz) accelerations obtained as forward wave propagation from our dynamic model. We de-convolved BB observed accelerograms by the site effects functions described in Appendix A, by assuming that there is no amplification below 1Hz, to get BB bedrock ground motions. We can notice that the de-convolved waveforms for stations SMNH10 and SMN002 seem to contain large site effects below 1Hz, which are not well reproduced in our simulated ground motions. The reason for this difference is because our ground motion simulations are based on a very simple velocity model (Table 1), that may largely differ from the actual velocity structure for this area.

Regarding the spectral characteristics of the simulated waveforms, in Figure 11 we plot the Acceleration Fourier spectra for the inverted HF ground motions (blue) and compare it with the site-effect corrected observed spectra (red). As seeing in this figure, the spectral amplitudes of simulated ground motions are in good agreement with the observed spectra, and that our HF radiation model based on fault rupture dynamics is able to reproduce for all sites, the ω^{-2} radiation (in displacement) at high frequencies predicted by the theory.

Directivity effect in radiation patterns

The directivity factor in equation (12) strongly modifies the conventional double-couple radiation pattern by introducing information about the dynamic fault rupture process. In Figure 12 we plotted the distribution of the directivity factor $(1- \Delta V_r \cos\psi/\beta_{max})^{-1}$ across the fault plane for three stations at different locations around the fault. The figure shows in a yellow to red scale the subfaults that amplify the directivity effect, and in a blue scale the subfaults that reduce this effect. In general a large contribution to the directivity originates from subfaults where ΔV_r approaches β_{max} , and where the angle between the rupture front propagation and the subfault-station take-off ray (ψ) is relatively small. For station OKYH08 for instance there is a large contribution to directivity from points located near the rupture front focusing region at the in-plane rupture front side earlier described, as in this region ΔV_r is large and ψ relatively small (Figure 12a). For stations OKYH08 and SMN002 it is clear that only the rupture front approaching the stations makes a contribution to the directivity, specially in regions propagating predominantly in mode II and with a large ΔV_r (Figures 12a and 12b). For station SMNH02 the contribution of the directivity factor is very small as angle ψ is close to $\pi/2$ for the majority of points within the fault plane (Figure 12c). Interestingly for this station most of the contribution to directivity originates within the anti-plane (mode III) rupture front approaching the surface. The distribution of directivity factors at these stations is in agreement with the results obtained for envelope amplitudes discussed previously.

In Figure 13 we plot the radiation pattern coefficient of the EW component across the fault plane for different stations and frequencies, without including the directivity effect (equation 13). These coefficients were obtained by tracing all subfault-station rays for the velocity model in Table 1 and applying a frequency dependent smoothing to the double-couple radiation pattern coefficients as the frequency increases (equation 13). We may observe that as the frequency augments the radiation patterns evolve from a variable to a completely uniform coefficient at 5Hz (F^{ave}=0.45). This smoothing in the radiation pattern is intended as mentioned in the strong motion simulation section to account for the scattering effect from small-scale heterogeneous structure in the near source region.

In Figure 14 we plot the radiation pattern distribution across the fault plane at the same stations and component as in Figure 13 but including the directivity factor (equation 12). We can observe that the radiation pattern incorporates in this case information about the dynamic rupture process such as the strong changes in rupture velocity as well as the rupture front focusing. We also note that for this radiation pattern model the signature of the rupture process still remains at 5Hz. We have shown in a previous section that the assumption of a radiation pattern model that gets completely uniform above this frequency leads to an underestimation of the observed amplitudes at most stations subjected to forward directivity. Therefore we may conclude that our model of a radiation pattern model that incorporates a directivity factor based on a dynamic fault rupture process, is appropriate to simulate directivity effects in HF ground motions.

Discussion and Conclusions

In this study we investigated the HF radiation during the 2000 Tottori earthquake based on a 3D spontaneous fault rupture dynamic model of the earthquake. Our model generalizes the HF radiation mechanism from a rupture speed discontinuity in a 2D crack and a suddenly stopping circular crack (Madariaga, 1977), to the radiation from a general 3D rupture in a planar fault, where HF is radiated during gradual changes of rupture velocity at the rupture front. Our dynamic rupture based HF radiation model indicates that strong HF radiation from the source is confined to regions where the product between stress drop and rupture velocity changes is large. In case of the Tottori earthquake we have obtained that this product is maximum at the rupture front focusing region above the hypocenter, which originates from a locally stronger patch above the hypocenter (barrier) that produces a strong deceleration and bending of the rupture front.

In order to test our HF radiation model we obtained independent estimates of HF radiation during the Tottori earthquake from near-source ground motion envelopes inversion. The results of our inversion show that the incorporation of a dynamic-based HF radiation model to the strong motion simulation lead to significant improvement in fitting of observed near-source ground motion envelopes, as compared to models without heterogeneity in rupture velocity. Our results from inversion show that significant HF radiation during the Tottori earthquake originated from a region less than a 20% of the total asperity area (large stress drop areas). We think that this characteristic is the most robust result from inversion and might be applicable to other earthquakes. These results have very important implications for strong motion modeling, as many current approaches for strong motion simulation assume that HF ground motion is radiated from the entire asperity area, without an appropriate consideration regarding fault rupture heterogeneity. Our inversion results show that location and amplitude of HF radiation regions during the Tottori earthquake are reasonably well resolved features from inversion. Our model is able to reproduce the ω^{-2} seismic radiation observed in near-source ground motions, in agreement with theoretical predictions for 2D ruptures.

Our results highlight the large influence of rupture propagation complexity from dynamic models into the near-source strong ground motion. This complexity basically results from the assumptions of parameters that define the friction law and the stress state prior to earthquake. Unfortunately our knowledge of these parameters for real earthquakes is very limited, that in consequence give origin to the non-uniqueness of physically-based models. Only through a combination of insights from dynamic models, experimental and theoretical studies of friction and observation from real earthquakes we would be able to reduce that non-uniqueness. Future works in this direction will have to be considered. But in the short-time, an alternative to address this problem is to make use of the kinematic models available to constraint the dynamic simulations as we did in the present work. Certainly this assumption is highly controversial because it has been shown that the kinematic inversions so far developed in the literature, have problems of resolution and non-uniqueness (e.g. Monelli and Mai 2008), which means that various kinematic models are able to produce good agreement with observations. This problem of kinematic models results in a high level of uncertainly on the kinematic parameters, therefore the dynamic parameters derived from the kinematic model would also carry this level of uncertainty, even though the ground motion from the dynamic model would also have good agreement with observations. Perhaps the use of multiple kinematic rupture models that satisfy the observations can reduces the uncertainties in kinematic parameters and therefore into the estimation of dynamic parameters. This problem is topic for a future work, for now it is out of the scope of the present paper, since the main purpose of our paper is to present the idea of how to incorporate results of a dynamically consistent rupture model (a physical model) into the high frequency ground motion estimation. In that way we are able satisfy the observations on the basis of a well-defined physical assumption of friction model. This approach might be more appropriate than simply assuming an arbitrary choice of input data without any physical constraints on the causative source physics. Once we reach to the level of well resolved kinematic models, the procedure to estimate dynamic parameters adopted in our work would allow us to reliably incorporate observational constraints into the dynamic model, which is the main difficulty of current dynamic models.

The development of dynamic models based on kinematic models addresses the problem of predicting dynamic parameters such as stress drop, strength excess (relative strength to rupture) to fit ground motion and outer-scale kinematic parameters such as final slip distribution and moment magnitude of a given earthquake. These kind of dynamic models are essentially an extension of kinematic models, but within the framework of dynamically consistent model of rupture. For example, Dalguer et al., (2008) developed dynamic models in the context of this idea, and propose, in statistical sense, stress drop distribution characteristic for different earthquake type and earthquake size that fit characteristics of past earthquakes. In the same manner, other relevant parameters such as the strength excess, whose strong influence on the HF radiation has been demonstrated in this paper, can also be calibrated and characterized.

Our results show that incorporation of a directivity factor based on a dynamic fault rupture process, leads to a significant improvement in fitting of observed waveform envelopes, as compared to the fitting obtained from a completely uniform radiation pattern model at high frequencies. The contribution of directivity to waveforms amplitudes originates from points in the fault plane where rupture velocity changes approach the S-wave velocity, and for stations where the take-off ray makes an acute angle with the local rupture propagation direction.

We proposed a HF radiation model based on local rupture velocity variations, derived from a 3D dynamic model of a planar fault with heterogeneity in friction law and stress. Other possible mechanisms for HF radiation have been recently proposed in the literature, such as the ω^{-2} radiation from fault kinks for a 2D anti-plane rupture (Madariaga et. al. 2006), as well as a crack coalescence mechanism for 2D in-plane ruptures (Kame and Uchida, 2008).

Other studies on the Tottori earthquake have reported more complexities not considered in this paper, which may also contribute to the HF radiation, such as: i) fault complexity, Fukuyama et. al. (2003) reported that the faulting of the Tottori earthquake took place in a multiple segments fault; ii) off-fault cracking, numerical studies of Dalguer et al (2003) and observations made by Fusejima et al (2000) show that off-fault cracking have been developed during the Tottori earthquake.

Therefore more studies are required to fully understand the complex radiation from 3D fault ruptures, that accounts in addition to the heterogeneity in friction law parameters considered in this paper, complex fault geometries, off-fault cracking and rupture front interactions.

Incorporation of rupture features from dynamic models into HF ground motion simulation and/or inversions lead to improvement in the fitting of observed seismograms, but the most important, the simulations satisfy observations on the basis of well-defined physical models. We show that the development of dynamic models for real earthquakes provides a means of testing HF ground motion simulation methods, so that we can develop improved HF models with greater predictive power for simulating ground motion from future earthquakes.

In the present study we have not explicitly included the effect of curvature of the rupture front which can be very important for the generation of caustics (wave front focusing) arising from a strong bending of the rupture front, as well as the curvature effect on the 3D geometrical diffraction of the seismic waves (Achenbach and Harris 1978). These combined effects might have a significant contribution to the HF ground motion radiation. Another simplification of our paper is the representation of the rupture velocity changes by using the divergence of rupture velocities from the dynamic model. A more complete description of ΔV_r would require the calculation of a second order gradient tensor of the rupture velocity field. These topics will be addressed in further studies.

In this paper we have estimated the stress intensity factor k (equation 6) by the envelope inversion. However we are aware that some trade-off between ΔV_r and k might occur as their product is used to calculate the HF radiation factor Ω. To avoid this problem it may be useful to make direct estimates of k from results of the 3D dynamic model. This also can be an interesting subject for future research.

Data and Resources

The strong motion data used for this study was provided by the K-NET/KiK-net networks at NIED. All the computations for this study were performed in an HP/GS1280, Alpha workstation at NIED. We used a Genetic Algorithm program (Chipperfield et. al. 1994) and Matlab MPI (Kepner and Ahalt 2004) for inversion. Some figures were drawn using the GMT software (Wessell and Smith 1998).

Acknowledgments

We thank Raul Madariaga and Luis Rivera for insightful discussions. We also thank Martin Mai for very helpful comments and suggestions and to Michel Bouchon and an anonymous referee for thorough reviews that contributed to largely improve the manuscript. This study was conducted under the Kakenhi grant No. 185404428, and under the NIED project "Strong Motion Prediction and Seismic Hazard Evaluation".

References

Achenbach, J. D., and J. G. Harris (1978). Ray Method for Elastodynamic Radiation From a Slip Zone of Arbitrary Shape, *J. Geophys. Res.*, 83, 2283-2291.

Aki, K. and P. Richards, 2002. Quantitative Seismology, Second Edition, *University Science Books*.

Andrews, D. J. (1976). Rupture velocity of plane strain shear cracks, *J. Geophys. Res.*, 81, 5679-5689.

Aochi, H. and K. Olsen (2004). On the Effects of Non-planar Geometry for Blind Thrust Faults on Strong Motion, *Pure appl. Geophys.* 161, 2139-2153.

Aoi, S., T. Kunugi, and H. Fujiwara (2004). Strong-Motion Seismograph Network Operated by NIED: K-NET and KiK-net, *Journal of Japan Association for Earthquake Engineering*, 4, 65-74.

Boatwright, J. (1982). A dynamic model for far-field acceleration, *Bull. Seism. Soc. Am.* 72, 1049-1068.

Boore D. M., and J. Boatwright (1984). Average body-wave radiation coefficients, *Bull. Seism. Soc. Am.* 74, 1615-1621.

Boore D. M. (2003). Simulation of Ground Motion Using the Stochastic Method, Pure appl. geophys., 160, 635-676.

Cocco, M., and J. Boatwright (1993). The envelopes of acceleration time histories, *Bull. Seism. Soc. Am.* 83, 1095-1114.

Chipperfield, A., P. Fleming, H. Pohlheim, and C. Fonseca (1994). Genetic Algorithm Toolbox for use with Matlab, User's Guide, Department of Automatic Control and Systems Engineering, University of Sheffield, 91pp.

Dalguer L.A, K. Irikura, J. Riera, and H.C. Chiu (2001). The Importance of the Dynamic Source Effects on Strong Ground Motion During the 1999 Chi-Chi (Taiwan) Earthquake: Brief Interpretation of the Damage Distribution on Buildings. *Bull. Seismol. Soc. Am.* 95, 1112-1127.

Dalguer, L. A., K. Irikura, W. Zhang, and J. D. Riera (2002). Distribution of Dynamic and Static Stress Changes during 2000 Tottori (Japan) Earthquake: Brief Interpretation of the Earthquake Sequences; Foreshocks, Mainshock and Aftershocks, *Geophys. Res. Lett.*, 29(16), 1758, doi:10.1029/2001GL014333.

Dalguer, L.A; K. Irikura and J. Riera, (2003). Generation of New Cracks Accompanied by the Dynamic Shear Rupture Propagation of the 2000 Tottori (Japan) Earthquake, *Bull. Seismol. Soc. Am.*, 93, 2236-2252.

Dalguer, L. A., and S. Day (2007). Staggered-grid split-node method for spontaneous rupture simulation, *J. Geophys. Res.*, 112, B02302, doi:10.1029/2006JB004467.

Dalguer L.A, H. Miyake, S. Day and K. Irikura (2008). Surface-rupturing and Buried Dynamic Rupture Models Calibrated with Statistical Observations of Past Earthquakes, *Bull. Seismol. Soc. Am.* **98**, 1147-1161, doi: 10.1785/0120070134.

Das S., and B. Kostrov (1983). Breaking of a single asperity: Rupture process and seismic radiation, *J. Geophys. Res.*, 88, 4277-4288.

Day, S.M. (1982). Three-dimensional simulation of spontaneous rupture: the effect of nonuniform prestress, *Bull. Seismol. Soc. Am.,* **72**, 1881-1902.

Day, S., L. A. Dalguer, and N. Lapusta (2005). Comparison of finite difference and boundary integral solutions to three-dimensional spontaneous rupture, *J. Geophys. Res.*, 110, B12307, doi:10.1029/2005JB003813.

Dunham, E., P. Favreau, and J. M. Carlson (2003). A Supershear Transition Mechanism for Cracks, *Science* 299, 1557.

Dunham, E., and R. Archuleta (2005). Near-source ground motion from steady state dynamic rupture pulses, Geophys. Res. Lett. 32, L03302, doi:10.1029/2004GL021793.

Fukuyama, E., and R. Madariaga, (2000). Dynamic Propagation and Interaction of a Rupture Front on a Planar Fault, *Pure appl. geophys.*, 157, 1959-1979.

Fukuyama, E., W. L. Ellsworth, F. Waldhauser, and A. Kubo (2003). Detailed Fault Structure of the 2000 Western Tottori, Japan, Earthquake Sequence, *Bull. Seismol. Soc. Am.*, 93, 1468–1478.

Fusejima, Y., T. Yoshioka, K. Mizuno, M. Shishikura, R. Imura, T. Komatsubara, and T. Sasaki (2000). Surface rupture associated with the 2000 Tottori-ken Seibu earthquake, Annual Report on Active Fault and Paleoearthquake Researches, No. 1, Geological Survey of Japan, National Institute of Advanced Industrial Science and Technology.

Guatteri, M., P. M. Mai, G. C. Beroza, and J. Boatwright (2003). Strong Motion Prediction from Stochastic-Dynamic Source Models, *Bull. Seism. Soc. Am.* 93, 301-313.

Guatteri, M., P. M. Mai, G. C. Beroza (2004). A Pseudo-Dynamic Approximation to Dynamic Rupture Models for Strong Motion Prediction, *Bull. Seism. Soc. Am.* 94, 2051-2063.

Hartzell, S., S. Harmsen, A. Frankel, and S. Larsen (1999). Calculation of Broadband Time Histories of Ground Motion: Comparison of Methods and Validation using Strong-Ground Motion from the 1994 Northridge Earthquake, *Bull. Seism. Soc. Am.* 89, 1484-1504.

Hartzell, S., M. Guatteri, P. M. Mai, P. C. Liu, and M. Fisk (2005). Calculation of Broadband Time Histories of Ground Motion, Part II: Kinematic and Dynamic Modeling Using Theoretical Green's Functions and Comparison with the 1994 Northridge Earthquake, *Bull. Seism. Soc. Am.* 95, 614-645.

Herrero, A., and P. Bernard (1994). A Kinematic Self-Similar Rupture Process for Earthquakes, *Bull. Seism. Soc. Am.* 84, 1216-1228.

Hisada, Y. (2000). A Theoretical Omega-Square Model Considering the Spatial Variation in Slip and Rupture Velocity, *Bull. Seism. Soc. Am.* 90, 387-400.

Hisada, Y. (2001). A Theoretical Omega-Square Model Considering the Spatial Variation in Slip and Rupture Velocity. Part 2: Case for a Two-Dimensional Source Model, *Bull. Seism. Soc. Am.* 91, 651-666.

Horike, M. (2006). Improvement of the stochastic method by introduction of the scattering effects in a simple way, Abstracts Japan Geoscience Union Meeting 2006, S111-003.

Ida Y. (1972). Cohesive Force across the Tip of a Longitudinal-Shear Crack and Griffith's Specific Surface Energy, *J. Geophys. Res.*, 20, 3796-3805.

Ide, S., and M. Takeo (1997). Determination of constitutive relations of fault slip based on seismic wave analysis, *J. Geophys. Res.*, 102, 27379-27391.

Irikura, K., and K. Kamae (1994). Estimation of strong ground motion in broad-frequency band based on a seismic source scaling model and empirical Green's function technique, *Annali di Geophysica* XXXVII, 1721-1743.

Iwata, T., H. Sekiguchi, Y. Matsumoto, H. Miyake, and K. Irikura, 2000. Source Process of the 2000 Western Tottori Prefecture Earthquake and Near-Source Strong Ground Motions, *Fall Meeting of the Seismological Society of Japan*.

Kakehi, Y., and K. Irikura (1996a). Estimation of high-frequency wave radiation areas on the fault plane by the envelope inversion of acceleration seismograms, *Geophys. J. Int.* 125, 892-900.

Kakehi, Y., K. Irikura, and M. Hoshiba (1996b). Estimation of High-frequency Wave Radiation Areas on the Fault Plane of the 1995 Hyogo-ken Nanbu Earthquake by the Envelope Inversion of Acceleration Seismograms, *J. Phys. Earth* 44, 505-517.

Kakehi, Y., and K. Irikura (1997). High-Frequency Radiation Process during Earthquake Faulting – Envelope Inversion of Acceleration Seismograms from the 1993 Hokkaido-Nansei-Oki, Japan, Earthquake, *Bull. Seism. Soc. Am.* 87, 904-917.

Kamae, K., K. Irikura and A. Pitarka, 1998. A Technique for Simulating Strong Ground Motion Using Hybrid Green's Function, *Bull. Seism. Soc. Am.* 88, No. 2, 357-367.

Kame N., and K. Uchida, 2008. Seismic radiation from a dynamic coalescence and the reconstruction of dynamic source parameters on a planar fault, *Geophys. J. Int.*, (accepted)

Kato, N. (2007). How Frictional Properties Lead to Either Rupture-Front Focusing or Cracklike Behaviour, *Bull. Seism. Soc. Am.,* 97, 2182-2189, doi:10.1785/0120070073.

Kepner, J., and S. Ahalt (2004). MatlabMPI, *Journal of Parallel and Distributed Computing*, 64, 997-1005.

Liu, P., R. Archuleta, and S. Hartzell (2006). Prediction of Broadband Ground-Motion Time Histories: Hybrid Low/High-Frequency Method with Correlated Random Source Parameters, *Bull. Seism. Soc. Am.,* 96, 2118-2130.

Madariaga, R. (1977). High-frequency radiation from crack (stress drop) models of earthquake faulting, *Geophys. J. R. astr. Soc.* 51, 625-651.

Madariaga, R. (1983). High-frequency radiation from dynamic earthquake fault models, *Ann. Geophys.* 1, 17-23.

Madariaga, R., J.P.Ampuero and M. Adda-Bedia (2006). Seismic Radiation From Simple Models of Earthquakes, Earthquakes: Radiated Energy and the Physics of Faulting, Geophysical Monograph Series 170, American Geophysical Union, 223-236.

Mai, P. M., and G.C. Beroza (2003). A hybrid method for calculating near-source, broadband seismograms: application to strong motion prediction, *Phys. Earth Planet. Inter.* 137, 183-199.

Mikumo, T., K. Olsen, E. Fukuyama, and Y. Yagi (2003). Stress-Breakdown Time and Slip-Weakening Distance Inferred from Slip-Velocity Functions on Earthquake Faults, *Bull. Seism. Soc. Am.* 93, 264-282.

Miyake, H., T. Iwata, and K. Irikura (2003). Source Characterization for Broadband Ground-Motion Simulation: Kinematic Heterogeneous Source Model and Strong Motion Generation Area, *Bull. Seism. Soc. Am.* 93, 2531-2545.

Miyatake, T. (2000). Computer Simulation of Strong Ground Motion near a Fault Using Dynamic Fault Rupture Modeling: Spatial Distribution of the Peak Ground Velocity Vectors, *Pure appl. Geophys.* 157, 2063-2081.

Monelli, D. and P.M. Mai (2008). Bayesian inference of kinematic earthquake rupture parameters through fitting of strong motion data, *Geophys. J. Int.,* **173**(1), 220-232

Moya, A, and K. Irikura (2003). Estimation of Site Effects and Q Factor Using a Reference Event, *Bull. Seism. Soc. Am.*, 93, 1730-1745.

Nakahara, H., T. Nishimura, H. Sato, and M. Ohtake (1998). Seismogram envelope inversion for the spatial distribution of high-frequency energy radiation from the earthquake fault: Application to the 1994 far east off Sanriku earthquake, Japan, *J. Geophys. Res.*, 103, 855-867.

Nakahara, H., T. Nishimura, H. Sato, M. Ohtake, S. Kinoshita, and H. Hamaguchi (2002). Broadband Source Process of the 1998 Iwate Prefecture, Japan, Earthquake as Revealed from Inversion Analyses of Seismic Waveforms and Envelopes, *Bull. Seism. Soc. Am.* 92, 1708-1720.

Oglesby, D., and S. Day (2002). Stochastic Fault Stress: Implications for Fault Dynamics and Ground Motion, *Bull. Seism. Soc. Am.* 92, 3006-3021.

Ohnaka, M. (2000). A Physical Scaling Relation Between the Size of an Earthquake and its Nucleation Zone Size, *Pure appl. geophys.* 157, 2259-2282.

Ohnaka, M. (2003). A constitutive scaling law and a unified comprehension for frictional slip failure, shear fracture of intact rock, and earthquake rupture, *J. Geophys. Res.*, 108(B2), 2080, doi:10.1029/2000JB000123.

Page, M., E. Dunham, and J. M. Carlson (2005). Distinguishing barriers and asperities in near-source ground motion, *J. Geophys. Res.* 110, B11302, doi:10.1029/2005JB003736.

Pitarka A., P. Somerville, Y. Fukushima, T. Uetake and K. Irikura, 2000. Simulation of Near-Fault Strong-Ground Motion Using Hybrid Green's Function, *Bull. Seism. Soc. Am.* 90, No. 3, 566-586.

Pulido, N., and K. Irikura (2000). Estimation of Dynamic Rupture Parameters from the Radiated Seismic Energy and Apparent Stress, *Geophysical Research Letters*, *27*, 3945-3948.

Pulido, N., and T. Kubo (2004). Near-fault strong motion complexity of the 2000 Tottori earthquake (Japan) from a broadband source asperity model, *Tectonophysics*, 390, 177-192.

Pulido, N., A. Ojeda, A. Kuvvet, and T. Kubo (2004). Strong Ground Motion Estimation in the Marmara Sea Region (Turkey) Based on a Scenario Earthquake, *Tectonophysics*, 391, 357-374.

Sato, T. (1994). Seismic Radiation from Circular Cracks Growing at Variable Rupture Velocity, *Bull. Seism. Soc. Am.* 84, 1199-1215.

Satoh, T. (2002). Radiation pattern and fmax of the Tottori-ken Seibu earthquake and the aftershocks inferred from KiK-net strong motion records, J. Struct. Constr. Eng., AIJ, 556, 25-34.

Somerville, P., K. Irikura, R. Graves, S. Sawada, D. Wald, N. Abrahamson, Y. Iwasaki, T. Kagawa, N. Smith, and A. Kowada (1999). Characterizing crustal earthquake slip models for the prediction of strong ground motion, *Seismol. Res. Lett.*, 70, 59-80.

Sorensen, M.B., K. Atakan, and N. Pulido (2007a).Simulated strong ground motions for the great M9.3 Sumatra-Andaman earthquake of 26 December 2004, *Bull. Seism. Soc. Am.* 97, S139-S151.

Sorensen, M.B., N. Pulido, and K. Atakan (2007b).Sensitivity of ground-motion simulations to earthquake source parameters: A case study for Istanbul, Turkey, *Bull. Seism. Soc. Am.* 97, 881-900.

Spudich P. and L. N. Frazer (1984). Use of ray theory to calculate high-frequency radiation from earthquake sources having spatially variable rupture velocity and stress drop, *Bull. Seism. Soc. Am.* 74, 2061-2082.

Rice, J. R. (2006). Heating and weakening of faults during earthquake slip, *J. Geophys. Res.*, 111, B05311, doi:10.1029/2005JB004006.

Tinti, E., P. Spudich, and M. Cocco (2005). Earthquake fracture energy inferred from kinematic rupture models on extended faults, *J. Geophys. Res.*, 110, B12303, doi:10.1029/2005JB003644.

Wessel, P. and W. H. F. Smith, 1998. New improved version of Generic Mapping Tools released, *EOS, Trans. Amer. Geophys. U.*, 79 (47), 579.

Zhang, W., T. Iwata, K. Irikura, H. Sekiguchi, and M. Bouchon (2003). Heterogeneous distribution of the dynamic source parameters of the 1999 Chi-Chi, Taiwan, earthquake, *J. Geophys. Res.*, 108(B5), 2232, doi:10.1029/2002JB001889.

Zeng, Y., K. Aki, and T. Teng (1993). Mapping of the High-Frequency Source Radiation for the Loma Prieta Earthquake, California, *J. Geophys. Res.*, 98, 11981-11993.

Zeng, Y., and J.G. Anderson (1996). A Composite Source Model of the 1994 Northridge Earthquake Using Genetic Algorithms, *Bull. Seism. Soc. Am.* 86, S71-S83.

Appendix A

Estimation of Site Effects Tottori earthquake

To infer the high frequency radiation from the observed waveforms of the Tottori earthquake, we should first correct the waveforms by the respective site amplifications, as our simulations of ground motion for the mainshock are performed for a hard-rock soil condition. For that purpose we calculate the site effects at several K-NET and KiK-net sites located within 40 km around the source area of the Tottori earthquake, by applying the "reference event" inversion methodology of Moya and Irikura (2003). That method allows the calculation of an "absolute" site amplification at a given station, which corresponds in fact to the amplification with respect to an average soil condition within the source area (β=3.5 km/s for the Tottori earthquake), as well as an average frequency dependent Q value around the source region. We modified the methodology of Moya and Irikura (2003) by incorporating the effect of path-independent loss of high frequency above f_{max}, as follows (see equation 1 of Moya and Irikura, 2003);

$$O_{ij}(f) = S_i(f)G_j(f)R_{ij}^{-1}e^{-\pi f R_{ij}/Q(f)\beta}P(f) \qquad \text{(A1)}$$

where O_{ij} is the observed spectra for the i event and j is the station, S_i is the source spectra for the i event, G_i is the site effect for the j station, and P is the path-independent loss of high frequency term as defined within equation 8, R_{ij} is the distance event-station, Q is the average anelastic attenuation of the region, and β is the average S-wave velocity in the source area. By taking the natural logarithm at both sides of equation A1 and rearranging terms we obtain an equation similar to equation 7 in Moya and Irikura (2003),

$$\ln\left[G_j(f)\right] - \frac{\pi f R_{ij}}{Q(f)\beta} = \ln\left[O_{ij(f)}\right] - \ln\left[S_i\right] - \ln\left[P\right] \qquad \text{(A2)}$$

but containing and additional term in the right side of the equation, corresponding to the logarithm of the high frequency attenuation filter P. Equation A2 is used as a constraint for the site effects inversion in the same way as equation 7 of Moya and Irikura (2003). Therefore the calculation of the site effects is performed in a similar manner as in Moya and Irikura (2003), with the only difference being the calculation of the additional term (*P*). The motivation for including term *P* in equation A1, is to avoid mapping the path independent loss of high-frequency effect into the solution space (site effects). Neglecting this term in equation A1 would yield unrealistic de-amplification values at high frequencies (frequencies higher than f_{max}), which would result in wrong corrections of the observed waveforms of the mainshock at high frequencies.

We estimated the site effects at 15 near source sites using 445 records, from 56 aftershocks with magnitudes ranging from 3 to 4.5. We use an average S-wave velocity value β of 3.5 km/s, a density of 2.7 T/m^3, and an average radiation pattern coefficient of 0.45. The resolved frequency range from inversion is between 1 and 30Hz. Below 1 Hz small S/N ratio of the waveforms makes the inversion results unstable. The source parameters of the reference events required by the inversion are summarized in Table A1.

To calculate $P(f)$ we use a equal to 8 and b equal to -0.5 (Boore 2003), and f_{max} equal to 10Hz, which is an average value for the aftershocks of the Tottori earthquake (Satoh 2002). We calculate separately the site effects for the EW and NS components. The results for the site amplification at the stations used for the dynamic model based HF ground motion simulations are shown in Figure A1. For most of the stations the two components show a similar amplification with frequency, except for station SMNH10 where the amplification of the EW component is much larger than the amplification of the NS component. The reason for this difference may be ascribed to 2D structural effects of the shallow sub-surface geology at this region. We obtained a frequency dependent attenuation value of $Q(f)=71.7f^{0.696}$ for the Tottori earthquake near-source region.

National Research Institute for Earth Science and Disaster Prevention, Japan (NIED), 3-1 Tennodai, Tsukuba, Ibaraki 305-0006, Japan, e-mail: nelson@bosai.go.jp
(NP)
Institute of Geophysics, ETH-Zurich, Switzerland
(LAD)

Tables

Table 1. Velocity model used for the dynamic model and strong motion simulation of the Tottori earthquake.

Depth (km)	Vp (m/s)	Vs (m/s)	ρ (T/m^3)
0	5500	3179	2.6
2	6050	3497	2.7
16	6600	3815	2.8
38	8000	4624	3.1

Table 2. Parameters for the dynamic fault rupture model of the Tottori earthquake.

Parameter	Value
LxW (km^2)	33 x 21
Fault strike, Dip	N150E, 90
Hypocenter (lon.lat.depth)	133.3527, 33.2679, 13.5 km
Depth fault upper edge (km)	0.2
Grid size (km)	0.2
Initial pre-stress (MPa)	70
Dc	20% of final slip
Total rupture time (s)	25
Fault discretization	331 x 211 nodes
Nucleation radius (km)	2
Time step (sec)	0.0065

Table 3. Parameters for the strong motion simulation of the Tottori earthquake.

Parameter	Value
Grid size (km)	1
Subfaults along strike, dip	33, 21
Sampling period (s)	0.01
Average S-wave velocity β (km/s)	3.5
Maximum S-wave velocity β_{max} (km/s)	3.8
Velocity model	see Table 1
Average density ρ (T/m^3)	2.7
Anelastic attenuation (Q)	$71.7f^{0.696}$ (Appendix A)
High frequency cut factors a, b	8, -0.5 (see eq. 11)
Radiation pattern frequencies f_1, f_2 (Hz)	1, 5 (see eq. 13)
Stress drop distribution ($\Delta\sigma$)	from dynamic model
Diffraction coefficient (D)	0.6 (see eq. 11)
Stress intensity factor coefficient (k)	0.13 (from inversion)
Rupture velocity changes (ΔV_r)	from inversion

Table A1. Reference events for the site effects inversion in the Tottori earthquake region.

Event	Mo (x10^{15} Nm)	f_c (Hz)
2000/10/06 23:13	1.84	2.87
2000/10/08 20:59	1.06	2.54
2000/10/17 22:17	2.84	1.15
2000/10/18 08:05	0.18	6.05
2000/11/03 16:33	5.23	0.50
2000/11/04 04:29	0.12	1.18
2000/11/05 03:00	0.31	2.11

Figure captions

Figure 1. Fault plane and mechanism of the 2000/10/06 Tottori-ken Seibu earthquake, Japan. K-NET/KiK-net stations used for high frequency radiation estimation are displayed.

Figure 2. Fault plane geometry and grid domain for the SGSN dynamic model of the Tottori earthquake.

Figure 3. (a) Final slip distribution from a dynamic model of the Tottori earthquake (grey scale), overlapped by the final slip from the kinematic model (white lines). Units are meters. (b) Dynamic stress drop distribution from the Tottori earthquake (color scale), overlapped by the strength excess distribution across the fault plane as white lines (in MPa).

Figure 4. (a) Rupture velocity distribution across the fault plane for the Tottori earthquake (grey scale)(in km/s), overlapped by the strength excess (white contour lines)(in MPa). Grey scale is discontinuous at a rupture velocity of 3.5 km/s, to separate sub-shear and super-shear ranges. (b) Index indicating the rupture mode across the fault plane of the Tottori earthquake. Values towards 1 correspond to a pure Mode II (in-plane) rupture and values towards zero a pure Mode III (anti-plane) rupture. Values in between correspond to a mixed rupture mode. Rupture front focusing region is the path labeled from point A to B. Rupture front is overlapped every 0.5s as black contour lines at each panel.

Figure 5. (a) Rupture velocity vectors across the fault plane of the Tottori earthquake, sampled every kilometer. A 2MPa barrier above the hypocenter is shown as a grey area. The vector lengths and color are scaled to rupture velocity amplitudes. We overlapped the location of the rupture front every 0.5s, as black contour lines. (b) A close-up of the rupture velocity vectors around the barrier, sampled every 200m. Location of the rupture front every 0.1s is displayed as black contour lines.

Figure 6. Schematic representation of the HF radiation from a 3D rupture front. Stress concentrations at the rupture front produced by a change in rupture velocity are shown. We also show the rupture length L defined in equation 6.

Figure 7. (a) Absolute value of rupture velocity changes distribution across the fault plane of the Tottori earthquake. Red values indicate accelerations of the rupture front and blue values represent deceleration or focusing of the rupture front. The color scale has been saturated for clarity of the figure (maximum and minimum values of rupture velocity changes are 4.87 km/s and -4.64 km/s respectively). Rupture front is overlapped every 0.5s as black contour lines. Rupture front focusing region is the path labeled from point A to B. (b) HF radiation factor (Ω) across the fault plane of the Tottori earthquake (equation 9). The stress drop is overlapped as black contour lines. The figure scale has been saturated for clarity (maximum value of Ω is 571 GPa $m^{3/2}s^{-1}$).

Figure 8. (a) Rupture velocity changes distribution across the fault plane of the Tottori earthquake, sampled every kilometer from the dynamic model (in km/s). (b) Rupture velocity changes distribution obtained from inversion of observed near-source waveform envelopes (in km/s). (c) Inverted HF radiation (Ω) of the Tottori earthquake across the fault plane. We overlapped the dynamic stress drop of the earthquake as black contour lines.

Figure 9. Observed (red) and Simulated (blue) HF acceleration envelopes (1 to 30Hz) at near-source stations (Figure 1), from the inverted HF radiation model of the Tottori earthquake. Dark blue envelopes correspond to simulations including directivity factor in radiation patterns, and dotted light blue lines correspond to simulations for a uniform radiation pattern at high frequencies. Scale of EW and NS components is the same for each station.

Figure 10. (a) Observed (red) and Simulated (blue) HF acceleration waveforms (EW and NS components) at several near-source stations of the Tottori earthquake used for HF inversion. Waveform amplitudes are displayed (cm/s/s) (b) Same as (a) but for broadband frequency accelerograms (0.1 to 30Hz).

Figure 11. (a) Observed (red) and Simulated (blue) HF acceleration Fourier spectra (EW and NS components) at near-source stations of the Tottori earthquake used for HF inversion. The horizontal line over the spectra within each panel shows the ω^0 radiation (ω^{-2} in displacement).

Figure 12. (a) Distribution of the directivity factor $(1- \Delta V_r \cos\psi/\beta_{max})^{-1}$ across the fault plane for the OKYH08 station. The figure shows in a yellow to red scale the subfaults that amplify the directivity effect, and in a blue scale the subfaults that

reduce this effect. (b) Same for SMN002 station, and (c) SMNH02 station. The minimum and maximum values of the directivity factor are displayed within each figure.

Figure 13. Radiation pattern coefficient of the EW component across the fault plane for several stations used for HF inversion of the Tottori earthquake, and for frequencies between f_1=1Hz and f_2=5Hz, without including the directivity factor (equation 13).

Figure 14. Radiation pattern coefficient of the EW component across the fault plane for several stations used for HF inversion of the Tottori earthquake, and for frequencies between f_1=1Hz and f_2=5Hz, including the directivity factor (equation 12).

Figure A1. Site effects for EW (black) and NS (grey) components at stations in the Tottori earthquake region, without including the free surface factor of 2. The last panel at the right-bottom shows the results of inversion for an average frequency dependent anelastic attenuation for the Tottori region ($Q(f)=71.7f^{0.696}$).

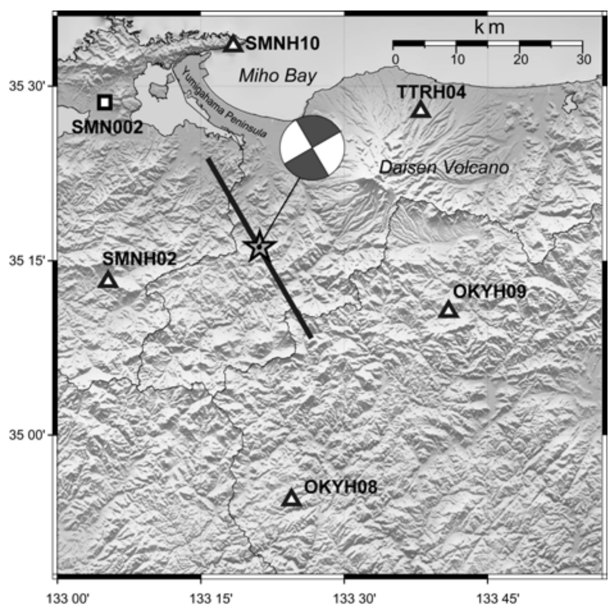

Figure 1

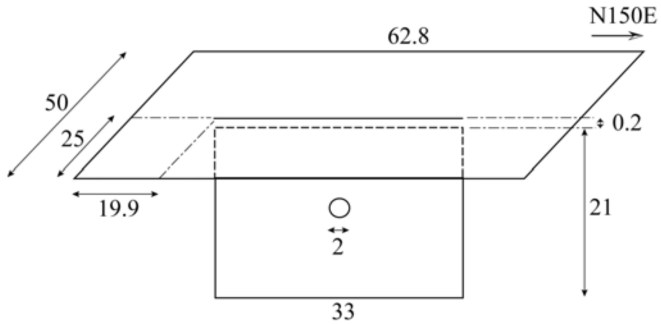

Figure 2

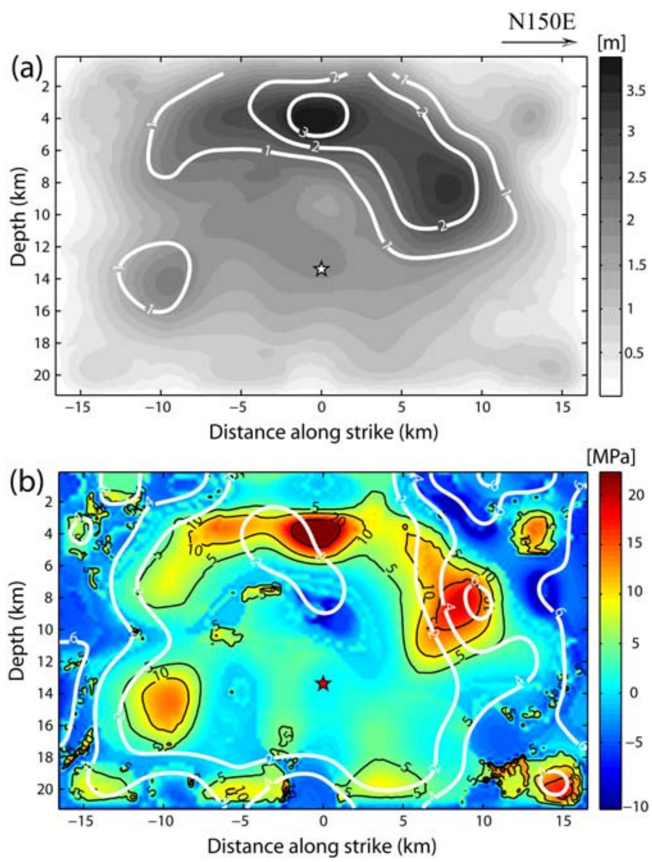

Figure 3

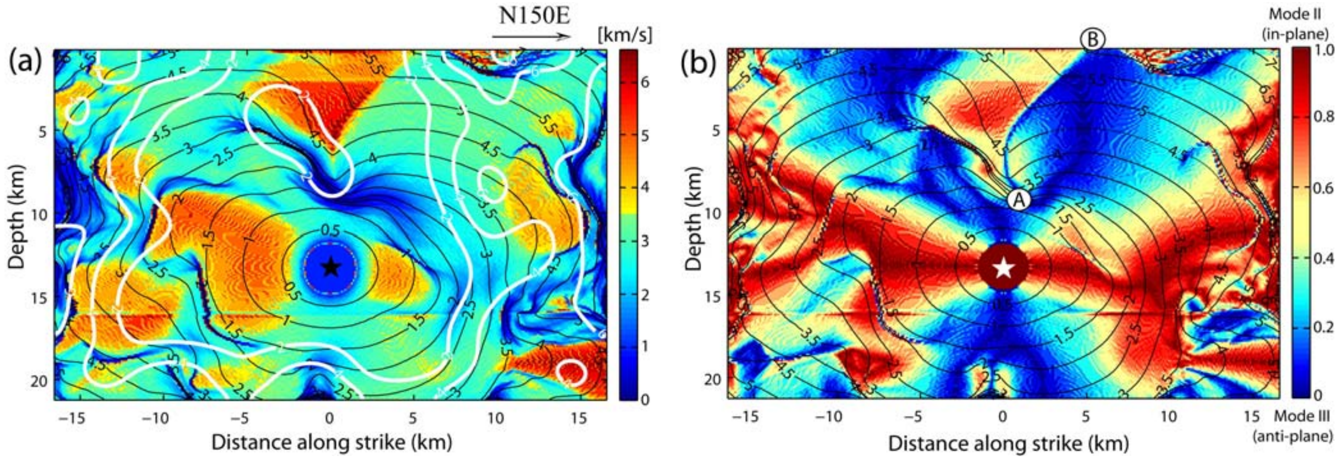

Figure 4

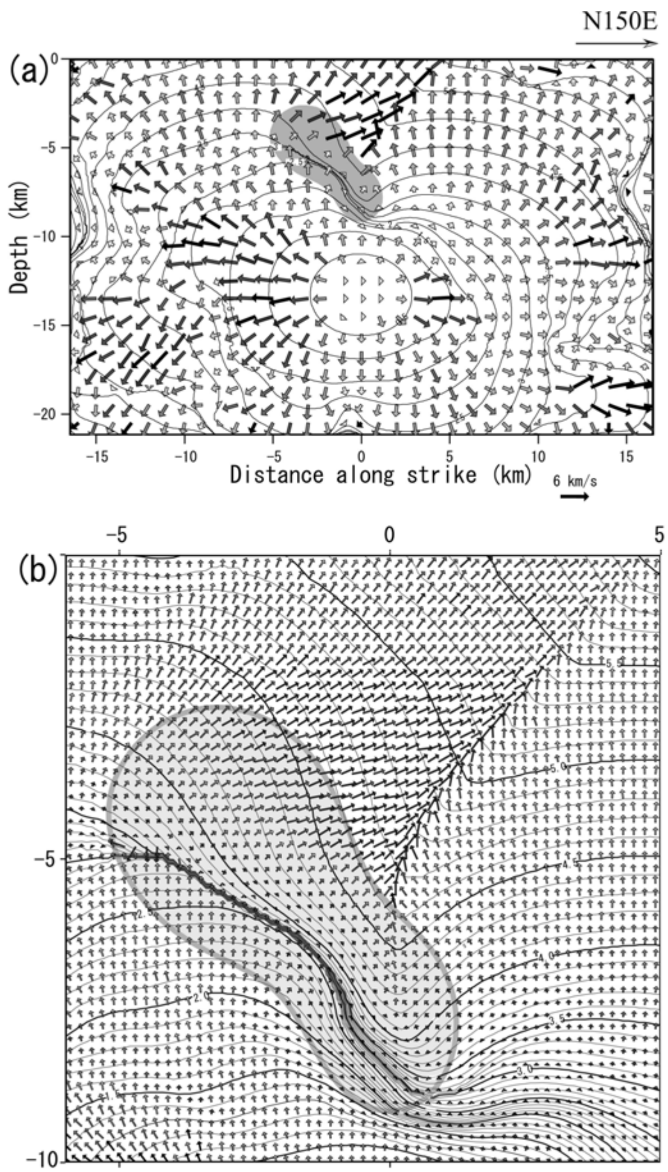

Figure 5

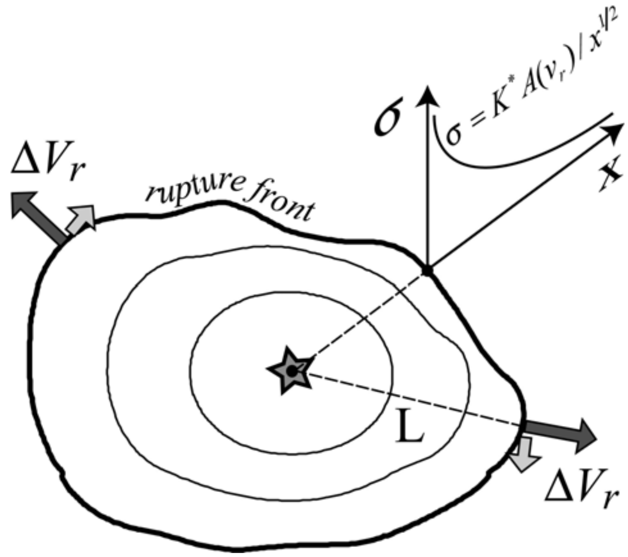

Figure 6

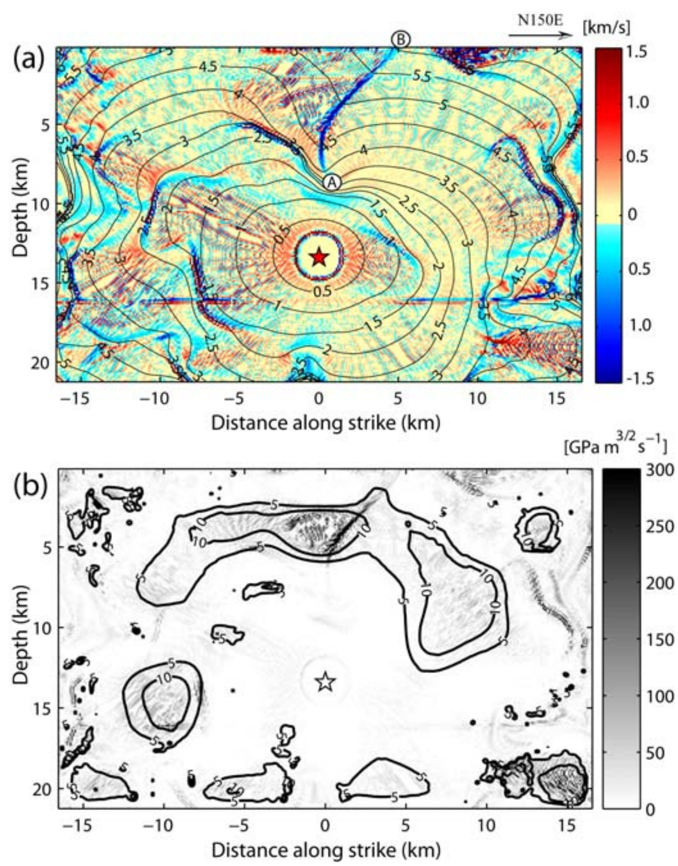

Figure 7

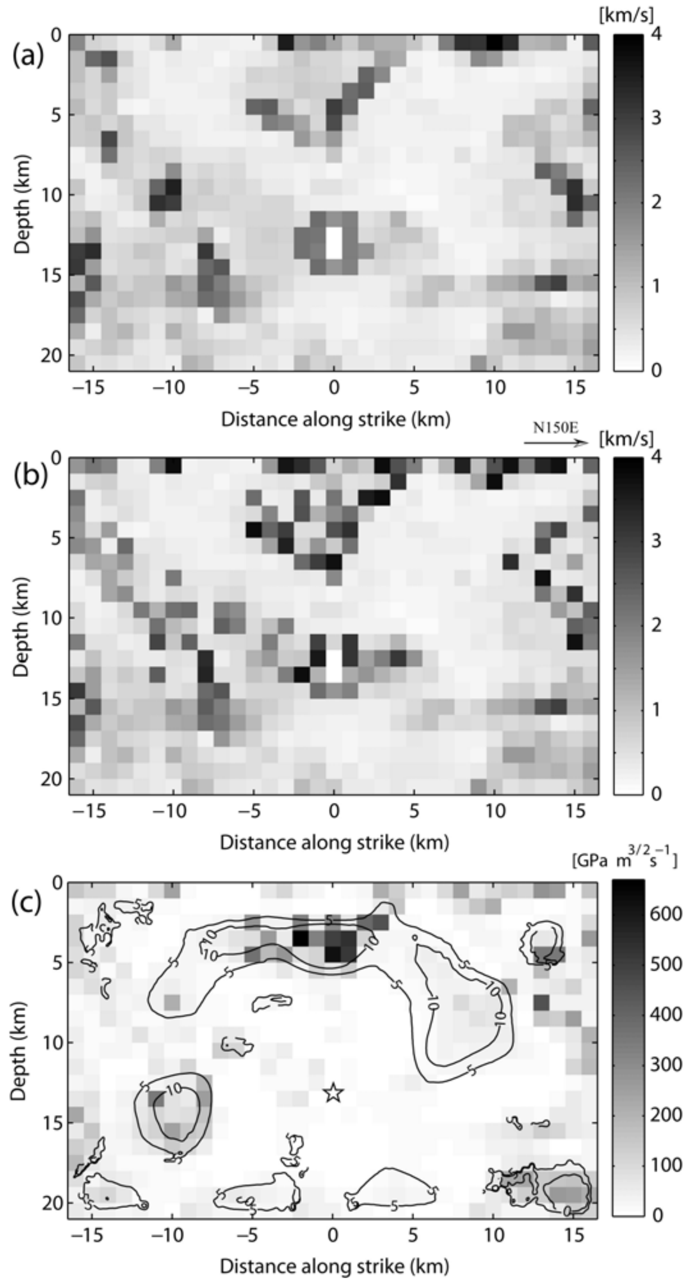

Figure 8

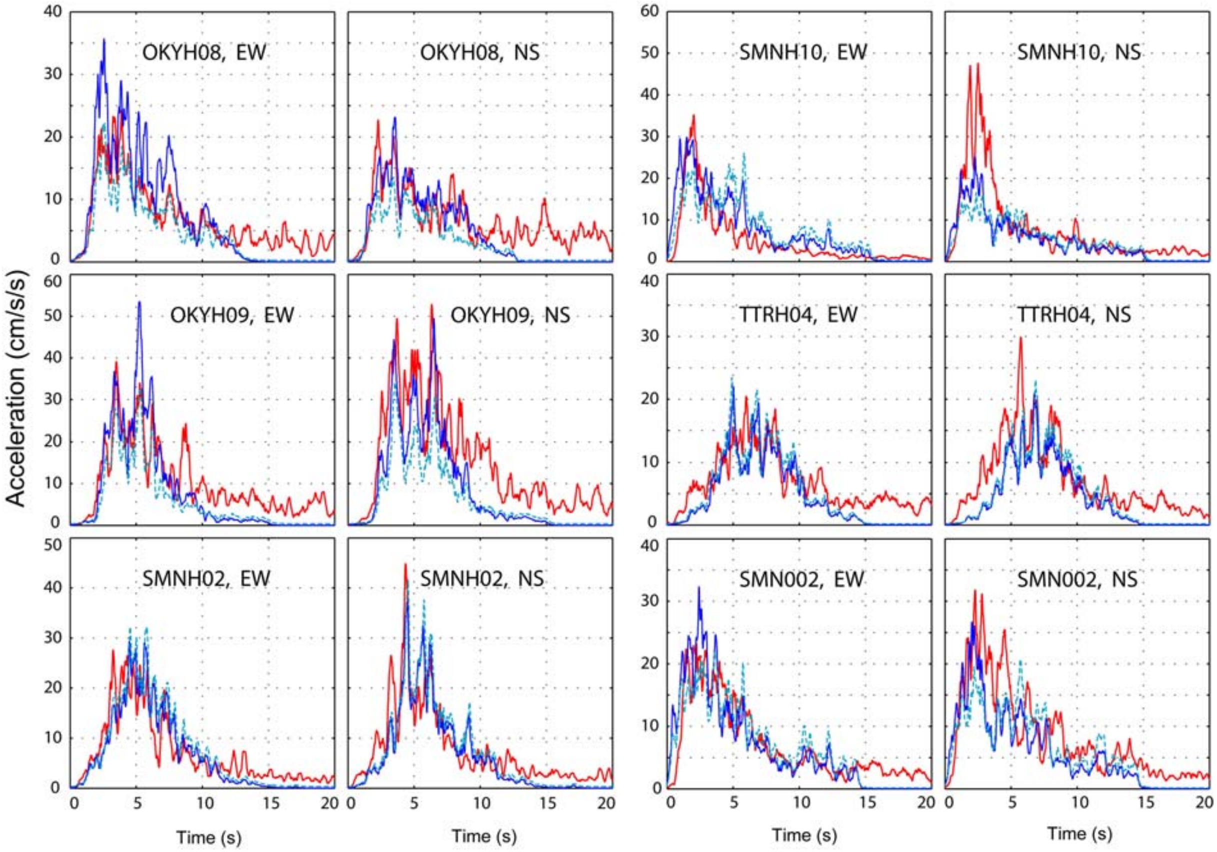
OKYH08, EW
OKYH08, NS
SMNH10, EW
SMNH10, NS
OKYH09, EW
OKYH09, NS
TTRH04, EW
TTRH04, NS
SMNH02, EW
SMNH02, NS
SMN002, EW
SMN002, NS
Acceleration (cm/s/s)
Time (s)

Figure 9

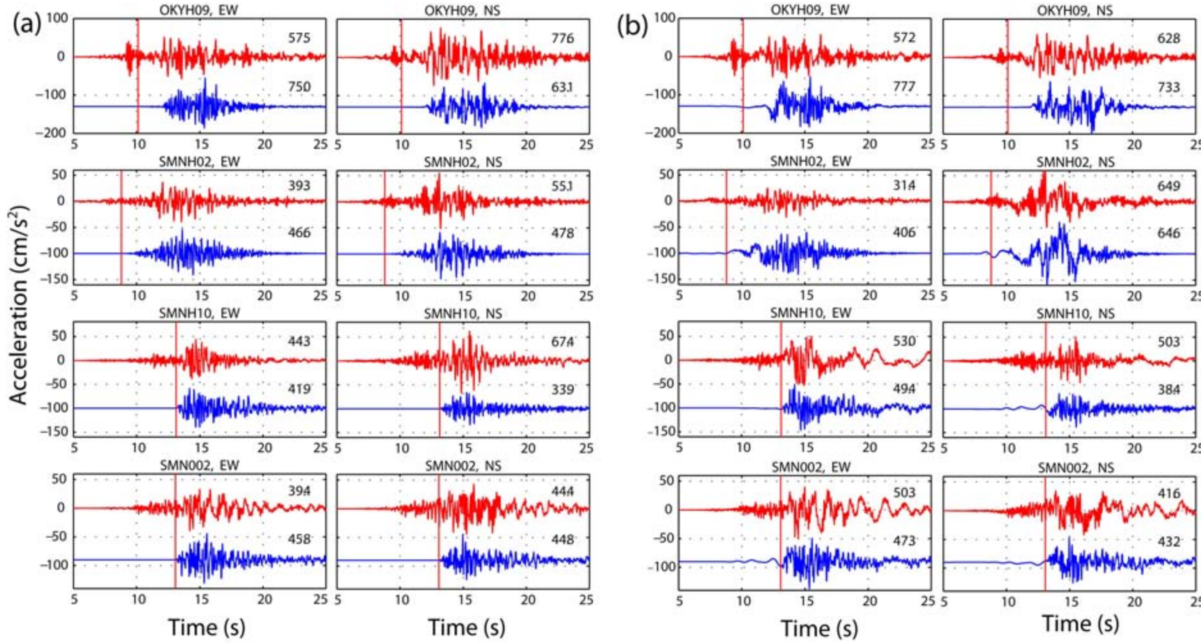

Figure 10

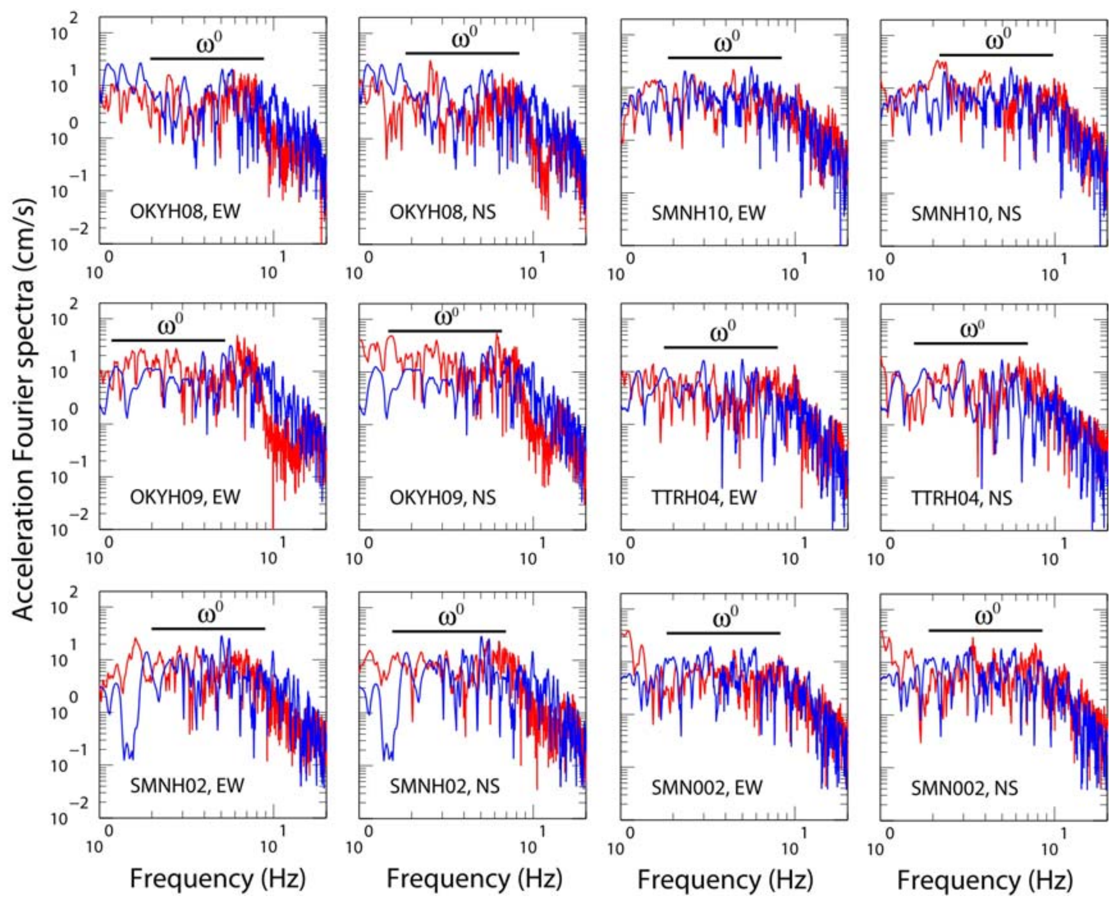

Figure 11

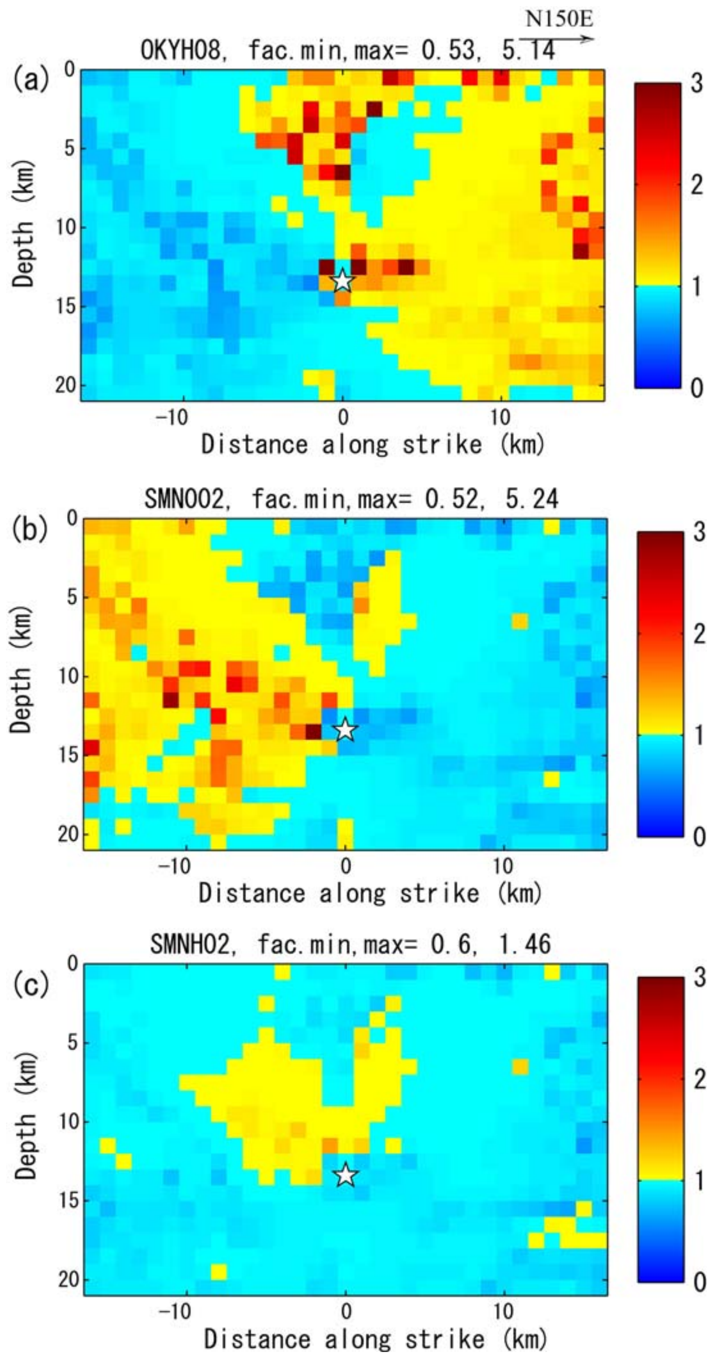
N150E
OKYH08, fac.min,max= 0.53, 5.14
(a)
Depth (km)
Distance along strike (km)
SMN002, fac.min,max= 0.52, 5.24
(b)
Depth (km)
Distance along strike (km)
SMNH02, fac.min,max= 0.6, 1.46
(c)
Depth (km)
Distance along strike (km)

Figure 12

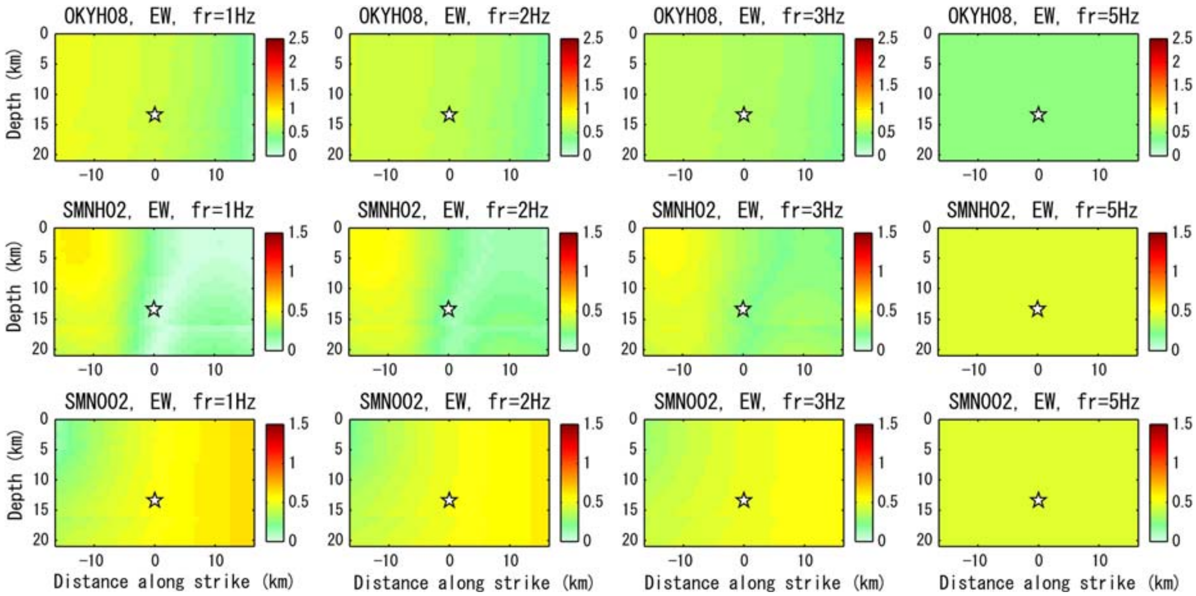

Figure 13

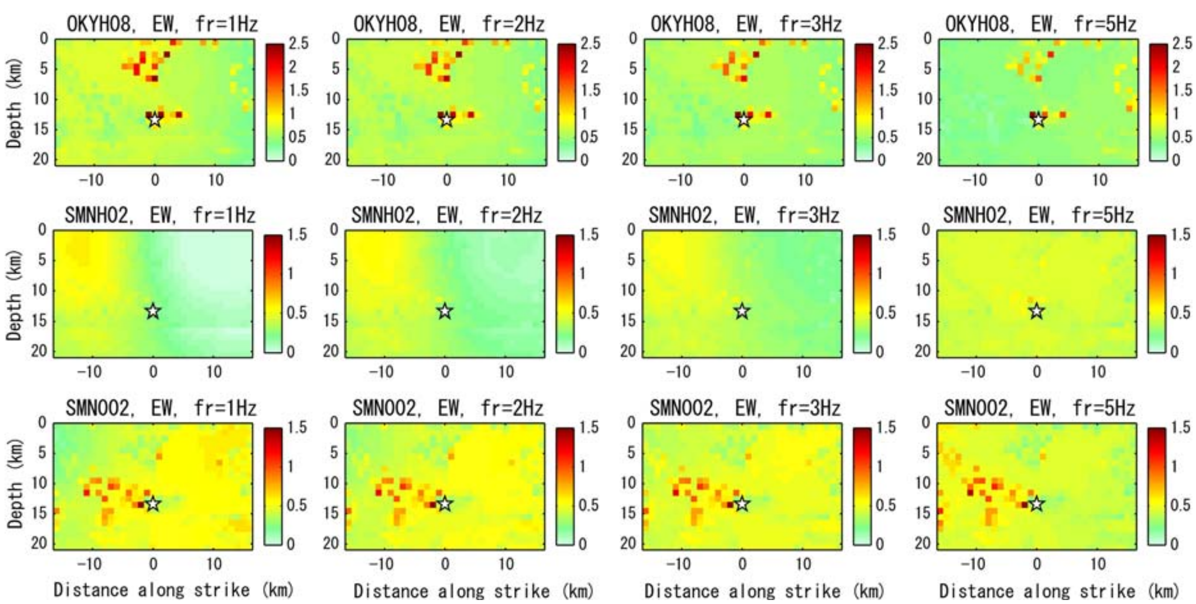

Figure 14

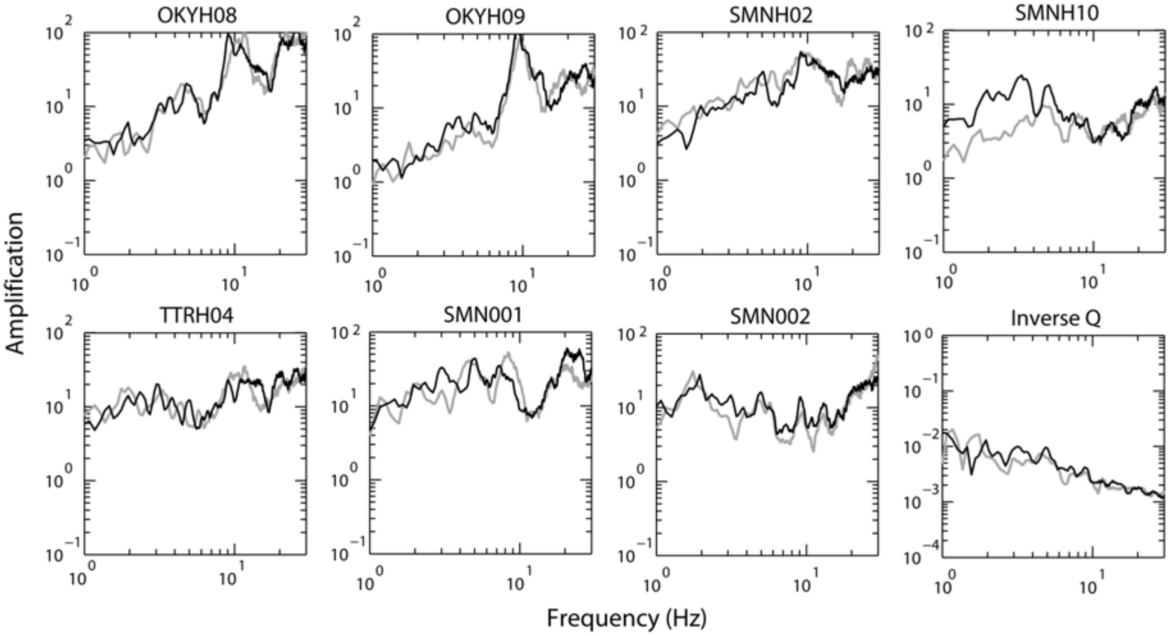
OKYH08
OKYH09
SMNH02
SMNH10
TTRH04
SMN001
SMN002
Inverse Q
Amplification
Frequency (Hz)

Figure A1